ADVANCED MATERIALS
www.advmat.de

Topological Spin Textures in a Non-Collinear Antiferromagnet System

Xionghua Liu, Qiyuan Feng, Dong Zhang, Yongcheng Deng, Shuai Dong, Enze Zhang, Weihao Li, Qingyou Lu,* Kai Chang, and Kaiyou Wang**

Topologically protected magnetic "whirls" such as skyrmions in antiferromagnetic materials have recently attracted extensive interest due to their nontrivial band topology and potential application in antiferromagnetic spintronics. However, room-temperature skyrmions in natural metallic antiferromagnetic materials with merit of probable convenient electrical manipulation have not been reported. Here, room-temperature skyrmions are realized in a non-collinear antiferromagnet, Mn_3Sn, capped with a Pt overlayer. The evolution of spin textures from coplanar inverted triangular structures to Bloch-type skyrmions is achieved via tuning the magnitude of interfacial Dzyaloshinskii–Moriya interaction. Beyond that, the temperature can induce an unconventional transition from skyrmions to antiferromagnetic meron-like spin textures at ≈220 K in the Mn_3Sn/Pt samples. Combining with the theoretical calculations, it is found that the transition originates from the temperature dependence of antiferromagnetic exchange interaction between kagome sublayers within the Mn_3Sn crystalline unit-cell. These findings open the avenue for the development of topological spin-swirling-based antiferromagnetic spintronics.

1. Introduction

Topologically protected magnetic textures (such as skyrmions and merons and their anti-particles), which are induced by chiral interactions between atomic spins in non-centrosymmetric magnetic compounds or in thin films with broken inversion symmetry, have been reported in several kinds of materials.[1–6] They are topological vortex-like objects surrounded by chiral boundaries, which can be stabilized by the Dzyaloshinskii–Moriya interaction (DMI) [7,8] and have been demonstrated great promise in nonvolatile memory or neuromorphic computing as solitonic information carriers.[9,10] Up to now, most investigations for topological spin textures are based on ferromagnetic materials.[1,11,12] Alternatively, designing and realizing these tiny whirls in antiferromagnetic materials and their heterostructures systems has recently become a fascinating issue in the condensed matter physics and information technology communities because of their nontrivial band topology and potential application in antiferromagnetic spintronics.[13]

The DMI in the bulk has beenreported to be more abundant in antiferromagnets than ferromagnets.[14] The topological antiferromagnetic states, once realized at room temperature, could be used for developing low-power nanospintronic devices.[13] Recently, the room-temperature stabilization of antiferromagnetic skyrmions has been reported in metal-based synthetic antiferromagnetic stacks.[15] Moreover, the stabilized antiferromagnetic half-skyrmions and bimerons at the interface between insulating α-Fe_2O_3 and Pt overlayer can be erased by magnetic fields and regenerated by temperature cycling.[16] However, topological spin textures such as skyrmions in natural metallic antiferromagnetic systems have not been reported. Therein searching for appropriate metallic antiferromagnetic

X. Liu, D. Zhang, Y. Deng, E. Zhang, W. Li, K. Chang, K. Wang
State Key Laboratory for Superlattices and Microstructures
Institute of Semiconductors
Chinese Academy of Sciences
Beijing 100083, P. R. China
E-mail: xionghualiu@semi.ac.cn; kywang@semi.ac.cn

X. Liu, D. Zhang, Y. Deng, E. Zhang, W. Li, K. Chang, K. Wang
Center of Materials Science and Optoelectronics Engineering
University of Chinese Academy of Sciences
Beijing 100049, P. R. China

Q. Feng, S. Dong, Q. Lu
Anhui Province Key Laboratory of Condensed Matter Physics at Extreme Conditions
High Magnetic Field Laboratory
Chinese Academy of Sciences
Hefei, Anhui 230031, P. R. China
E-mail: qxl@ustc.edu.cn

Q. Feng, S. Dong, Q. Lu
Hefei National Laboratory for Physical Sciences at the Microscale
University of Science and Technology of China
Hefei, Anhui 230026, P. R. China

K. Wang
Beijing Academy of Quantum Information Sciences
Beijing 100193, P. R. China

K. Wang
Center for Excellence in Topological Quantum Computation
University of Chinese Academy of Science
Beijing 100049, P. R. China

The ORCID identification number(s) for the author(s) of this article can be found under https://doi.org/10.1002/adma.202211634

DOI: 10.1002/adma.202211634

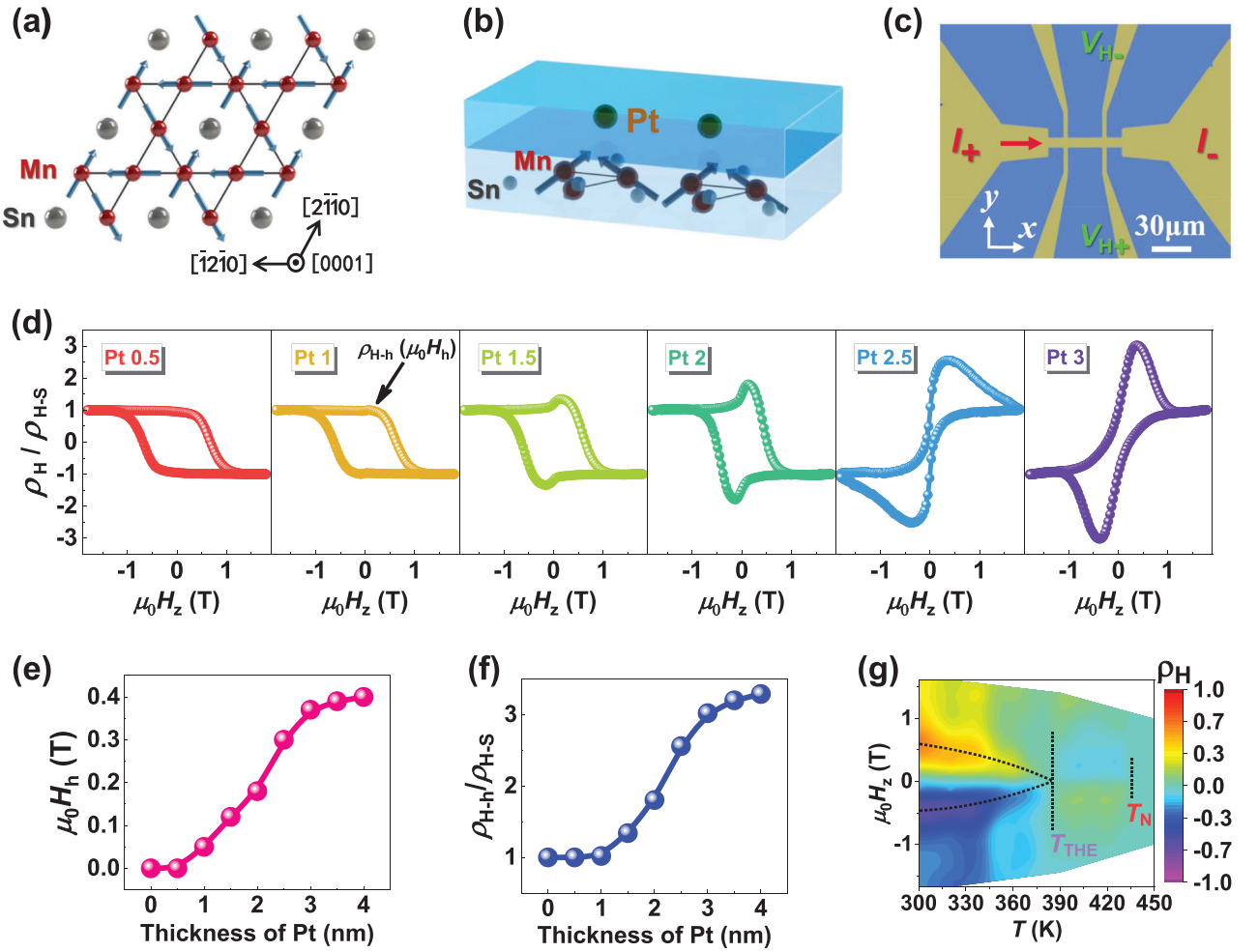

Figure 1. Magnetic structures, magnetotransport properties of the Mn_3Sn and Mn_3Sn/Pt devices. a) Triangular spin structure in the kagome layer of Mn_3Sn. b) Simplified schematic picture illustrating the Dzyaloshinskii–Moriya interaction (DMI) at the interface between an Mn_3Sn film and a heavy metal Pt. c) Optical microscopy image of our fabricated Hall device and measurement scheme. d) Evolution of normalized anomalous Hall resistivity vs $\mu_0 H_Z$ curves for the 60 nm-thick Mn_3Sn with various Pt overlayer thicknesses measured at RT. The anomalous Hall hump resistivity $\rho_{H\text{-}h}$ and Hall hump field $\mu_0 H_h$ are indicated by the arrow. e,f) The $\mu_0 H_h$ and the relative ratio of the $\rho_{H\text{-}h}$ to the $\rho_{H\text{-}S}$: $\rho_{H\text{-}h}/\rho_{H\text{-}S}$ as a function of Pt overlayer thickness. g) Color scale plot of ρ_H vs $\mu_0 H_Z$ curves at temperatures ranging from 300 to 450 K for Mn_3Sn (60 nm)/Pt (3 nm) sample. The transition temperature T_{THE} for the disappearance of the topological Hall effect, and the T_N are close to 390 K and 430 K, respectively (see Figure S3, Supporting Information).

materials and then rebuilding their spin textures would be strongly desirable.

The non-collinear antiferromagnetic Weyl semimetals such as Mn_3Sn, which combines the advantages of vanishing stray field and ultrafast spin dynamics as well as a large anomalous Hall effect and the chiral anomaly of Weyl fermions, can provide an ideal platform to explore the multifaceted physics of the interplay between band topology and magnetism as well as the emergent chiral swirling spin textures.[17–23] Mn_3Sn possesses an ABAB stacking sequence of the (0001) kagome lattice of Mn with a 120° spin structure and negative vector chirality of the in-plane Mn moments due to geometrical frustration below its Néel temperature (T_N) (**Figure 1**a).[19] Here we achieved room-temperature skyrmions in non-collinear antiferromagnet Mn_3Sn capped with a Pt overlayer system, in which a novel transition from skyrmions to antiferromagnetic meron-like spin textures at ≈220 K was also observed.

2. Results and Discussion

2.1. Interfacial DMI Induced Variable Spin Textures

To reconstruct the Mn spin textures of Mn_3Sn at room temperature (RT), we introduced the interfacial DMI with a Pt overlayer (Figure 1b).[1,24,25] Experiments were performed on sputter-deposited Ru (5)/Mn_3Sn (60)/Pt (t_{Pt})/AlO_x (3) (thickness in nanometers) thin films with t_{Pt} = 0.5, 1, 1.5, 2, 2.5, 3, 3.5 and 4 nm, and the reference samples consisting of Ru (5)/Mn_3Sn (t_{Mn3Sn})/AlO_x (3) and Ru (5)/Mn_3Sn (t_{Mn3Sn})/Pt (3)/AlO_x (3) with

t_{Mn3Sn} = 40, 50 nm, Ru (5)/Mn_3Sn (60)/Ir–Mn (2)/AlO_x (3), Ru (5)/Mn_3Sn (60)/Ir–Mn (2)/Pt (3)/AlO_x (3), and Ru (5)/Mn_3Sn (60)/AlO_x (t_{AlOx})/Pt (3)/AlO_x (3) with t_{AlOx} = 1 and 2 nm. All these samples were grown on thermally oxidized Si substrates at RT and then annealed in a vacuum (see Experimental Section for details). The XRD results of our Mn_3Sn film are presented in Section S1 and Figure S1 (Supporting Information). The quality of our polycrystalline Mn_3Sn thin films has been checked by microstructure characterizations, chemical composition, transport, and magnetic properties measurements in our previous work.[26]

The normalized anomalous Hall resistivity $\rho_H/\rho_{H\text{-}S}$ ($\rho_{H\text{-}S}$ is the positive saturation anomalous Hall resistivity) versus the out-of-plane magnetic field $\mu_0 H_Z$ for Mn_3Sn (60)/Pt (t_{Pt}) samples, measured at RT (Figure 1c), is exhibited in Figure 1d. Notably, centrosymmetric anomalous Hall humps are observed for the sample with 1-nm-thick Pt overlayer, see the Hall hump resistivity ($\rho_{H\text{-}h}$) indicated by the arrow. The Hall hump could originate from the variable spin textures that were caused when electrons gain a real-space Berry phase upon encountering a magnetic structure with nonzero scalar spin chirality,[27,28] or the spatial inhomogeneity in k-space Berry curvature generated two anomalous Hall effect channels,[29–31] of Mn_3Sn thin film.

Subsequently, we designed an experiment to corroborate that this hump-like anomaly of $\rho_H/\rho_{H\text{-}S}$ vs $\mu_0 H_Z$ curves in Figure 1d was indeed attributed to the spin-swirling object-induced topological Hall effect (THE), see Section S2 and Figure S2 in Supporting Information. With increasing Pt thickness, the anomalous Hall hump field $\mu_0 H_h$ and $\rho_{H\text{-}h}$ gradually increase (Figure 1e,f) and become nearly saturated for $t_{Pt} \geq 3$ nm, indicating the gradual enhancement of THE for thin Pt capping layer ($t_{Pt} <$ 3 nm).[1,24,25] Similar behaviors can be observed for different thick (40 and 50 nm) Mn_3Sn and their corresponding heterostructure devices (see Section S3 and Figure S3, Supporting Information). Therefore, the evolution of Mn spin from coplanar inverted triangular structures to swirling textures can be achieved via interfacial DMI tuning in our Mn_3Sn/Pt heterostructures. Besides, the transition temperature T_{THE}, corresponding to the disappearance of THE, and the T_N were found approximately to be 390 K and 430 K, respectively, for our Mn_3Sn (60)/Pt (3) sample (Figure 1g; Figure S4, Supporting Information).

2.2. Magnetic Force Microscopy Measurements

We employed real-space magnetic force microscopy (MFM) to examine the spin textures in our Mn_3Sn/Pt heterostructures. **Figure 2**a–f shows the RT MFM images taken during the field reversal process after 2T magnetization saturation. A full set of the MFM results can be found in Section S5 and Figure S5 (Supporting Information). One notes that the MFM images display complex mixed states of skyrmions and conventional magnetic domains produced by reversal of the antiferromagnetic phase (magnetic octupole).[32] To effectively separate these magnetic structures, we applied pixel-by-pixel subtraction operations to adjacent MFM images (see Figure 2g–i).[6,33] According to the Hall and magnetic property measurements in **Figure 2**j, we can further divide spin textures/behaviors into three regions: antiferromagnetic order region I (0 to −0.4 T, Figure 2g), The dominant region II (−0.4 to −1.0 T, Figure 2h), and magnetic saturated region III (<−1.0 T, Figure 2i).[20,34]

Figure 2g,h presents a well-defined domain contrast in red against a uniform cyan background. According to the difference in size, shape, and single lever of the spin features, we classify the domains into two categories: Type 1 and Type 2. Type 1 domains, as circled by the dotted line in Figure 2g, have rather irregular shapes with sizes ranging from several hundred nanometers to even micrometers and possess a relatively strong contrast, which could correspond to magnetic octupole domains.[32] As a sharp contrast, Type 2 domains have rather uniform and circular shapes and coincident magnitude (see the dashed line 1 in Figure 2h and revealed by the cross-sectional line in Figure 2k), which, mainly located in the region II, means the high correlation between Type 2 domains and topological Hall effect. These results strongly indicate that Type 2 MFM contrasts are induced by individual skyrmions.[6,15,35] For comparison, Figure 2i exhibits a vague weak magnetic contrast with red or cyan color each randomly occupying ≈50% of the image area, suggesting the saturation domain pattern with a further increasing magnetic field.

To further investigate the basic behaviors of skyrmions such as their emergence and annihilation, we performed additional two sets of MFM measurements on two randomly selected areas, which are presented in Figure 2l–n and Figure 2o–q, respectively. Note that the skyrmions emerge as the reversal of regular antiferromagnetic domains occurs with increasing the magnetic field, and then disappear when further enlarging the magnetic field. The cross-sectional line profiles of several representative skyrmions are summarized in Figure 2k, corresponding to the blue and red lines indicated in Figure 2h,p, respectively, and the full-width-at-half-maximum (FWHM) value of each skyrmion is labeled under each hump with the average FWHM of ≈100 nm. Here the observed size could be much larger than the real skyrmion diameter, affected by the factors such as the skyrmion stray field, effective size of the MFM tip, and effective lift height.[6] Therefore, the room-temperature skyrmions with a size of ≈80 nm can be demonstrated in our Mn_3Sn/Pt sample.[6]

2.3. Theoretical Simulations

To capture the underlying microscopic mechanism of skyrmions in our Mn_3Sn/Pt heterostructures, we carried out Monte Carlo simulations based on first-principles calculations. With well-relaxed interface structures, we performed a series of constrained first-principles calculations and derived corresponding parameters of the effective spin Hamiltonian, as well as numerical DMI parameters associated to each site of the magnetic atoms. The Heisenberg hamiltonian takes the conventions as:

$$E = -\sum_i K_i \vec{S}_i^2 - \sum_{i \neq j} \left[J_{ij}^{iso} \vec{S}_i \cdot \vec{S}_j + \vec{S}_i J_{ij}^{ani} \vec{S}_j + \vec{D}_{ij} \left(\vec{S}_i \times \vec{S}_j \right) \right] \quad (1)$$

where the first term indicates the single-ion anisotropy, the second and third terms are isotropic exchange and anisotropic exchange, and the last one represents the DMI.[36,37] Detailed information can be found in Experimental Section and Section S6 in Supporting Information.

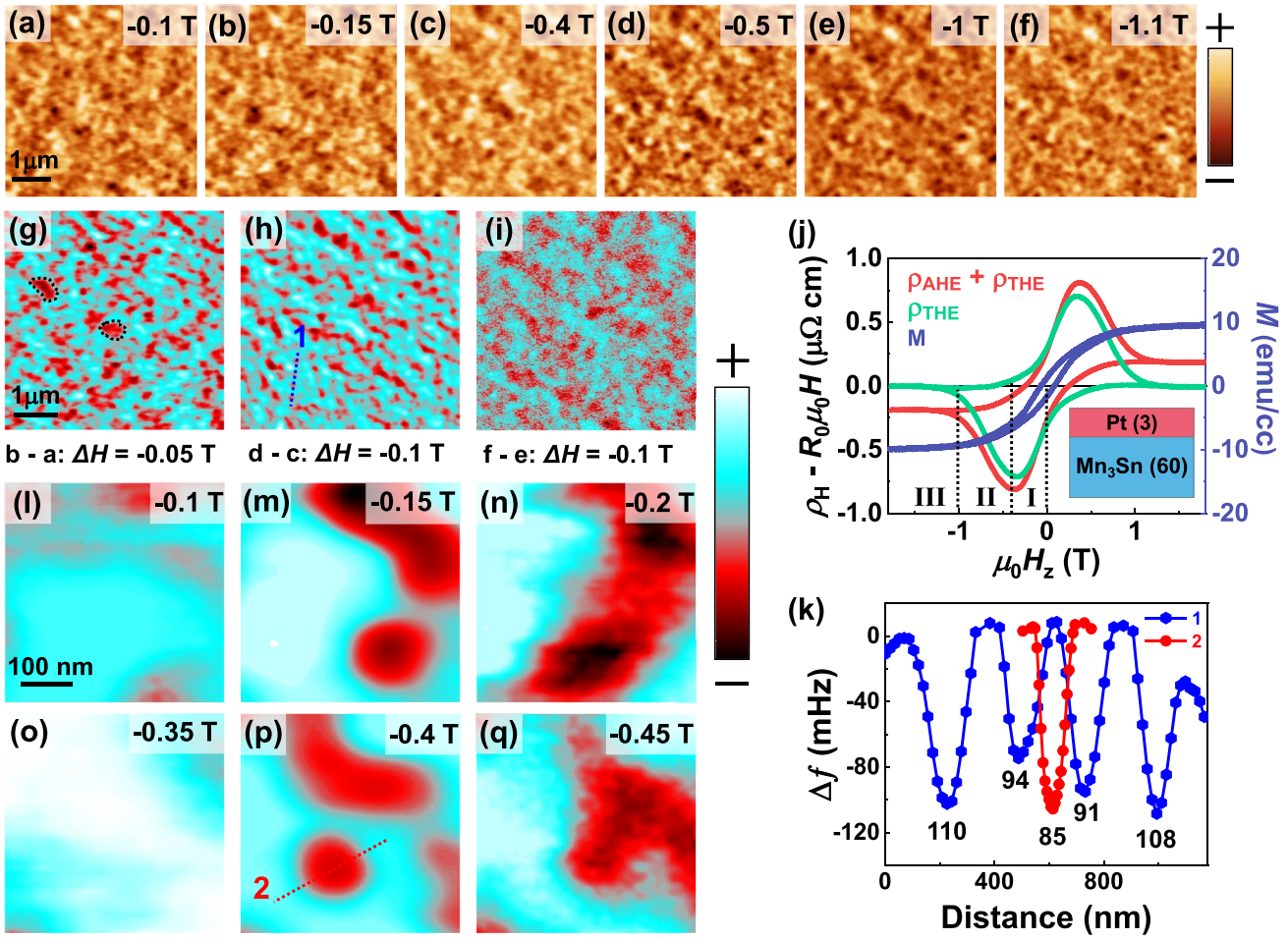

Figure 2. Magnetic force microscopy of room temperature skyrmions in Mn_3Sn (60 nm)/Pt (3 nm) sample. a–f) MFM images obtained in a field reversing process (field applied out-of-plane) at RT after saturation at 2 T. The scanning area is $5 \times 5\ \mu m^2$ and the scale bar is 1 μm. The whole set of the MFM images were obtained in exactly the same sample region to ensure the accuracy of the pixel-by-pixel subtraction operation. g–i) Processed MFM images obtained by applying a pixel-by-pixel subtraction operation to neighboring images ($g = b - a$; $h = d - c$; $i = f - e$). j) Hall resistivity and magnetization as a function of applied field at RT. k) Cross-sectional line profiles of 5 representative skyrmions. Line 1 and line 2 are obtained from Figure 2h,p, respectively. The FWHM value of each selected skyrmion is labeled under the hump and the average FWHM is ≈100 nm. (l–n) and (o–q) are two independent sets of MFM images obtained at two different locations. The scanning area is $420 \times 420\ nm^2$ and the scale bar is 100 nm. The color scales for (a–i) and (l–q) are 590, 580, 530, 440, 360, 370, 540, 570, 60 mHz and 200, 240, 230, 150, 200, 210 mHz, respectively.

We mainly focus on the crystalline direction [0001] because this direction is the preferential orientation for our Mn_3Sn film,[26] as well as the large lattice mismatch between Mn_3Sn and Pt for other directions will lead to weak DMI. **Figure 3**a shows the simulated contour plot of magnetization in the [0001] direction (M_Z) on a 30 × 30 nm^2 at equilibrium temperature, 300 K, the amplitude of the contour plot ranges from −2 to 2 because the constructing M_Z values are superpositions of sublayers A and B within the Mn_3Sn unitcell.[17–19] The detailed in-plane displacements of magnetization indicated with black arrows are displayed in Figure 3b,c, which possesses Bloch-type skyrmion features since the in-plane displacements are transversal to the flipping directions of M_Z.[1] Moreover, we got a typical size of the simulated skyrmion of ≈10 nm (Figure 3a). Considering unavoidable imperfections at the interface and polycrystalline character of our Mn_3Sn/Pt samples, the real DMI should be smaller than the theoretical prediction, correspondingly, the experimentally observed skyrmions should be larger since the size of the skyrmions is inversely proportional to the amplitude of the DMI strength.[38,39] Thus, one can find reasonable reproduction of skyrmions in Mn_3Sn/Pt heterostructures from our simulations.

Our theoretical simulations demonstrate that the equilibrium spin textures are strongly temperature dependent. The absence of skyrmions above 400 K (see Figure S8, Supporting Information) is well in agreement with the T_{THE} of ≈390 K for our Mn_3Sn (60)/Pt (3) sample (see Figure 1g; Figure S4, Supporting Information). The skyrmion patterns in Figure 3a are only robust within equilibrium temperatures from 200 to 400 K. At temperatures below 200 K, as the simulated results at 10 K shown in Figure 3f, the M_Z tends to be isotropic because the effective interlayer antiferromagnetic exchange interaction between kagome sublay-

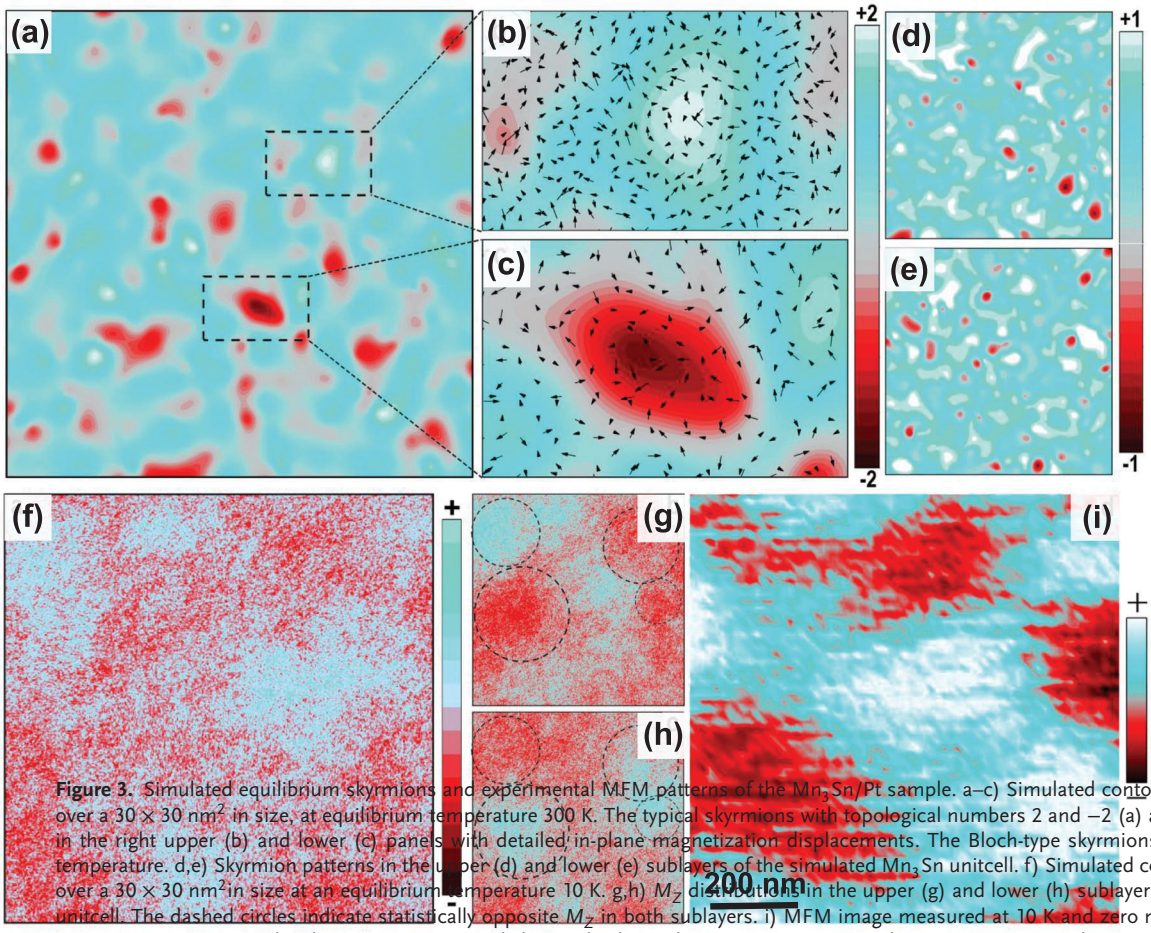

Figure 3. Simulated equilibrium skyrmions and experimental MFM patterns of the Mn_3Sn/Pt sample. a–c) Simulated contour plot of M_Z distribution over a 30 × 30 nm^2 in size, at equilibrium temperature 300 K. The typical skyrmions with topological numbers 2 and −2 (a) are zoomed in and shown in the right upper (b) and lower (c) panels with detailed in-plane magnetization displacements. The Bloch-type skyrmions can be observed at this temperature. d,e) Skyrmion patterns in the upper (d) and lower (e) sublayers of the simulated Mn_3Sn unitcell. f) Simulated contour plot of distribution over a 30 × 30 nm^2 in size at an equilibrium temperature 10 K. g,h) M_Z distributions in the upper (g) and lower (h) sublayers of the simulated Mn_3Sn unitcell. The dashed circles indicate statistically opposite M_Z in both sublayers. i) MFM image measured at 10 K and zero magnetic fields for Mn_3Sn (60 nm)/Pt (3 nm) sample. The scanning area, scale bar, and color scale are 1 μm, 200 nm, and 120 mHz, respectively.

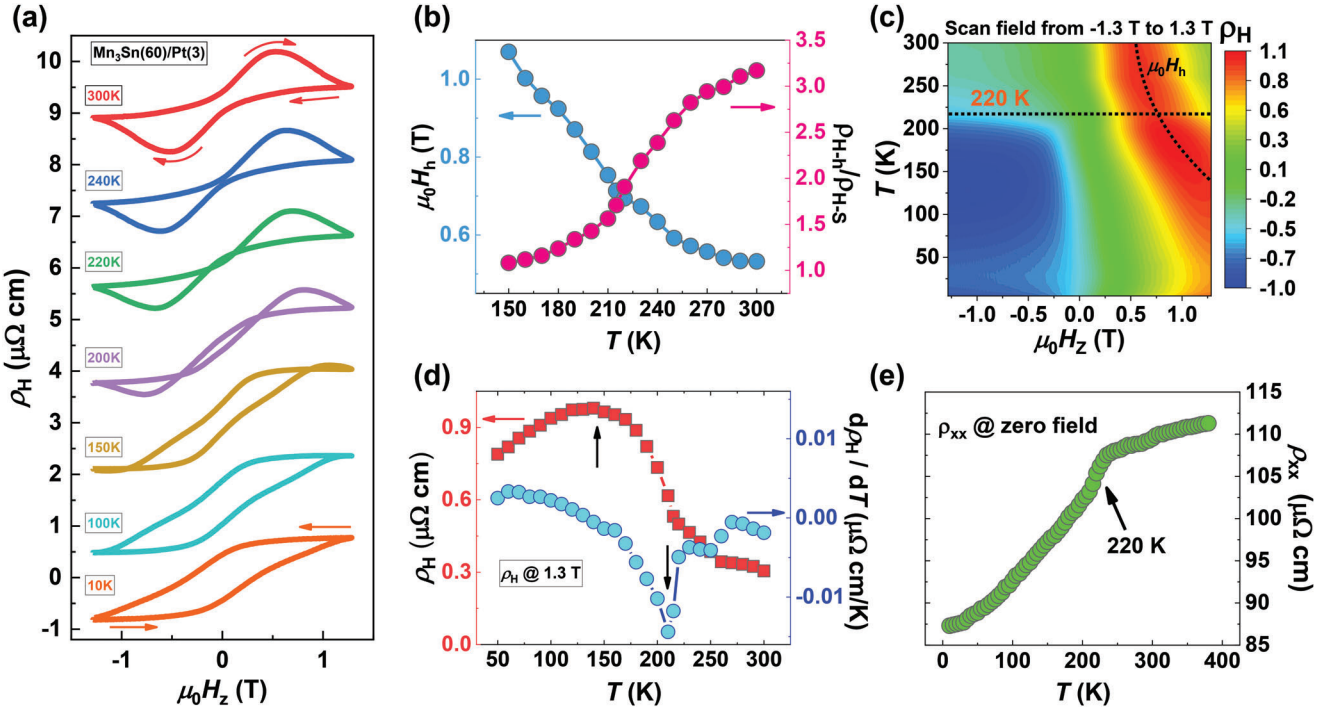

Figure 4. Temperature dependence of magnetotransport properties in Mn_3Sn (60 nm)/Pt (3 nm) sample. a) Anomalous Hall resistivity (ρ_H) as a function of $\mu_0 H_Z$ curves measured at different temperatures from 10 to 300 K. b) The anomalous Hall hump field $\mu_0 H_h$ and relative hump resistivity $\rho_{H\text{-}h}/\rho_{H\text{-}S}$ as a function of temperature from 150 to 300 K. The gradual reduction of $\mu_0 H_h$ and enhancement of $\rho_{H\text{-}h}/\rho_{H\text{-}S}$ can be observed with increasing temperature. c) Color scale plot of ρ_H vs $\mu_0 H_Z$ curves with scanning field from −1.3 to 1.3 T at temperatures from 10 to 300 K. A sharp variation of ρ_H at ≈220 K would be possibly associated to the transition from skrymions to like-meron spin texture. d) Temperature dependence of ρ_H measured at 1.3 T and its differential curve $d\rho_H/dT$. The largest ρ_H at ≈150 K and the largest variation of ρ_H, corresponding to minimum $d\rho_H/dT = -0.015$ μΩ cm K^{-1}, at ≈220 K can be observed. e) Longitudinal resistivity ρ_{xx} at zero magnetic field as a function of temperature. A rapid jump in ρ_{xx} at ≈220 K can be also observed.

ers (≈20 meV) overcomes thermal fluctuation. Correspondingly, the M_Z values are statistically opposite in large areas denoted by dashed circles for individual sublayers A (Figure 3g) and B (Figure 3h), respectively, which are quite different from the results at 300 K (Figure 3d,e). We then carried out the MFM measurements at 10 K and observed similar magnetization patterns (without skyrmions) (Figure 3i; Figure S6, Supporting Information) to the simulated results (Figure 3f). Importantly, this statistical opposition in M_Z values (Figure 3g,h) indicates the existence of antiferromagnetic meron-like spin textures,[40,41] which is in stark contrast to the skyrmions in ferromagnetic materials.[1,40,41] This unconventional transition from skyrmions to antiferromagnetic meron-like spin texture occurring in Mn_3Sn/Pt heterostructure results in the decrease or even disappearance of THE at low temperatures.

2.4. Temperature Dependence of Magnetotransport Properties

We then conducted the magnetotransport properties measurements at low temperatures to further verify our theoretically predicted transition from skyrmions to antiferromagnetic meron-like spin textures for our Mn_3Sn/Pt heterostructures. As shown in **Figure 4**a, with lowering temperature, THE revealed by ρ_H vs $\mu_0 H_Z$ curves indeed gradually weakens, corresponding to the gradual reduction of $\rho_{H\text{-}h}/\rho_{H\text{-}S}$ in Figure 4b. In particular, the anomalous Hall humps in ρ_H vs $\mu_0 H_Z$ curves cannot be observed below 150 K (The ρ_H vs $\mu_0 H_Z$ curve for pure Mn_3Sn at 10 K is shown in Figure S9, Supporting Information for comparison), meaning the probable formation of antiferromagnetic meron-like spin texture at this temperature range (the skyrmions and corresponding THE completely disappears), which is consistent with our theoretical prediction.

To obtain the transition temperature from skyrmions to antiferromagnetic meron-like spin texture, we plotted the color scale of ρ_H vs $\mu_0 H_Z$ curves with a scanning field from −1.3 to 1.3 T at temperatures from 10 to 300 K in Figure 4c. Obviously, a sharp variation of ρ_H at ≈220 K can be observed (as the dashed line indicated). Accordingly, the ρ_H vs temperature curve ρ_H vs T measured at 1.3 T exhibits a rapid jump and its corresponding differential curve $d\rho_H/dT$ gives a minimum value (−0.015 μΩ cm K^{-1}) at ≈220 K (Figure 4d). In addition, the longitudinal resistivity ρ_{xx} vs temperature curve ρ_{xx} vs T measured at zero magnetic field also presents a sharp change at ≈220 K (Figure 4e). These results suggest the transition temperature should be ≈220 K.

We note that the 220 K is higher than the temperature having disappearance of THE (below 150 K). The transition from skyrmions to antiferromagnetic meron-like spin texture occurring at a relatively wide temperature range would be a plausible scenario for our Mn_3Sn/Pt samples. The skyrmions play a dominant role at high temperatures, and then the antiferromagnetic meron-like spin texture appears at ≈220 K, corresponding to a

rapid decrease of THE (Figure 4b). With further decreasing temperature, more antiferromagnetic meron-like spin textures were formed, and ultimately became dominated spin textures below 150 K. This relatively wide temperature range for the transition could be owing to the polycrystalline character of our Mn_3Sn/Pt heterostructures.

3. Conclusions

We have achieved room-temperature skyrmions in non-collinear antiferromagnet Mn_3Sn capped with a Pt overlayer system, in which a novel transition from skyrmions to antiferromagnetic meron-like spin textures at ≈220 K was also found. The interlayer antiferromagnetic meron-like spin texture hosts some characters like that of the intralayer antiferromagnetic skyrmions (such as the disappearance of THE),[14,42] which not only offers a new type of antiferromagnetic-like skyrmions but also pave possible approaches to manipulate topological spin textures by tuning interlayer interactions via strain or intercalation, etc. Our findings demonstrate the rich variety of topological spin textures in non-collinear antiferromagnet heterostructure systems, which may promote the discovery of new topological spin textures in antiferromagnets.

4. Experimental Section

Sample and Device Fabrication: The samples used for realizing the room-temperature skyrmions in a non-collinear antiferromagnet system, which consisted of Ru (5)/Mn_3Sn (60)/Pt (t_{Pt})/AlO_x (3) (thickness in nanometers) thin films with t_{Pt} = 0.5, 1, 1.5, 2, 2.5, 3, 3.5, and 4 nm, were grown on thermally oxidized Si substrates, the bottom Ru layer and top AlO_x layer were used as the buffer layer and capping layer, respectively. For comparison, the reference samples consisting of Ru (5)/Mn_3Sn (t_{Mn3Sn})/AlO_x (3) and Ru (5)/Mn_3Sn (t_{Mn3Sn})/Pt (3)/AlO_x (3) with t_{Mn3Sn} = 40 and 50 nm, Ru (5)/Mn_3Sn (60)/Ir–Mn (2)/AlO_x (3), Ru (5)/Mn_3Sn (60)/Ir–Mn (2)/Pt (3)/AlO_x (3), and Ru (5)/Mn_3Sn (60)/AlO_x (t_{AlOx})/Pt (3)/AlO_x (3) with t_{AlOx} = 1 and 2 nm, were also deposited on Si/SiO_2 substrates. All the samples were grown at room temperature and then annealed at 450 °C for 30 min by using the vacuum annealing furnace (F800-35, East Changing Technologies, China) at a base vacuum of 2×10^{-7} Torr. The samples were patterned into Hall bar devices with a current channel width of 10 μm by using photolithography and Ar-ion etching (Figure 1c).

Magnetic and Magnetotransport Measurements: The magnetic measurements of our Mn_3Sn/Pt samples were carried out using a Quantum Design vibrating sample magnetometer (VSM). A reading current of I_{read} = 0.1 mA was used to measure the Hall resistivity ρ_H and the longitudinal resistivity ρ_{xx} of the Mn_3Sn/Pt Hall bar devices, as shown in Figure 1c. The electrical measurements were conducted at different temperatures using a cryogenic probe station (Lake Shore Cryotronics, Inc.).

Magnetic Force Microscopy (MFM): A home-built variable temperature MFM equipped with a 20 T commercial superconducting magnet (Oxford Instruments) was used. The design, measurement details, and contrast mechanism of the MFM could be found in reference.[43] In brief, an attractive (repulsive) force on the MFM tip gave rise to a negative (positive) frequency shift. For Mn_3Sn/Pt heterostructures, there was negligible force (attractive force) between the local moments of antiferromagnetic phase (skyrmions or ferromagnetic phase) and the MFM tip, which caused a bright contrast (dark contrast) in the MFM images. The conventional ferromagnetic phase and skyrmions could be further identified through their difference in size, shape, and single lever. Skyrmions possessed a uniform circular shape and a lower signal lever due to their unique swirling spin structure. MFM images were analyzed using Gwyddion software.

Theoretical Simulations: The interface effect was modeled by stacking Mn_3Sn with a thickness of 6 atomic layers onto a Pt substrate with a thickness of three atomic layers, along the crystalline direction [0001]. The Pt substrate possessed an in-plane lattice reconstruction of 2 × 2, meanwhile, the Mn_3Sn kept 1 × 1, since the perfect lattice match between the two materials. For simplicity, no interfacial defect nor interdiffusion was taken into the model, and a vacuum slab of 2 nm thick was incorporated to eliminate unphysical wavefunction hybridizations. The interface model was well relaxed before successive first-principles calculations. The first-principles calculations were performed in the framework of density functional theory using the Vienna Ab initio Simulation Package (VASP) [44,45] with the projected augmented wave (PAW) method.[46] The initial magnetic momentum of Mn atoms were fixed in chiral antiferromagnetic ordering and the spin–orbit coupling (SOC) effect was included both in the self-consistent and band structures calculations. The exchange-correlation potentials were treated with generalized gradient approximation using Perdew–Burke–Ernzerhof (PBE) functionals,[47] and the Kohn–Sham single-particle wave functions are simulated by plane-wave expansions with a cutoff of 500 eV. A 13 × 13 × 1 Γ-centered grid mesh was adopted in the irreducible reciprocal Brillouin zone of all the layered materials, in companion with a 10^{-6} eV criteria of the total energy convergency. With the converged first-principles calculations, parameters of the anisotropic Heisenberg spin Hamiltonians were derivated by combination of constraint DFT calculations and the TB2J package.[36] The Heisenberg Hamiltonian took the conventions as:

$$E = -\sum_i K_i \vec{S}_i^2 - \sum_{i \neq j} \left[J_{ij}^{iso} \vec{S}_i \cdot \vec{S}_j + \vec{S} J_{ij}^{ani} \vec{S}_j + \vec{D}_{ij} \left(\vec{S}_i \times \vec{S}_j \right) \right] \quad (2)$$

where the first term indicated the single-ion anisotropy, the second and third terms were isotropic exchange and anisotropic exchange, and the last one represented the DMI. At the skyrmion simulation stage, the magnetic atomic site associated numeric spin Hamiltonians were taken into the VAMPIRE code [48,49] as inputs, and Monte Carlo simulations in the field-cooling approach were performed. Each field-cooling Monte Carlo simulation was started from a reasonably high initial temperature of 600 K and down to selective equilibrium temperatures, such as 10, 200, 300, and 400 K, respectively.

Supporting Information

Supporting Information is available from the Wiley Online Library or from the author.

Acknowledgements

X.L., Q.F., and D.Z. contributed equally to this work. This work was supported by the National Key R&D Program of China (grant No 2022YFA1405102), the National Natural Science Foundation of China (grant No.s 12241405, 12174382, U1932216, 51627901, 12004386), the Chinese Academy of Sciences (grant No.s XDB28000000, XDB44000000), the Beijing Natural Science Foundation (grant No. 2212048), the Beijing Natural Science Foundation Key Program (grant No. Z190007), the Maintenance and Renovation Project for CAS (grant no. DSS-WXGZ-2019-0011), Hefei Science Center CAS (grant No.s 2020HSC-UE014, 2021HSC-UE010), High Magnetic Field Laboratory of Anhui Province, Anhui Lab of Adv. Photon Sci. and Tech.

Conflict of Interest

The authors declare no conflict of interest.

Data Availability Statement

The data that support the findings of this study are available from the corresponding author upon reasonable request.

Keywords

Dzyaloshinskii–Moriya interactions, non-collinear antiferromagnets, skyrmions, topological spin textures

Received: December 12, 2022
Revised: February 27, 2023
Published online:

[1] A. Fert, N. Reyren, V. Cros, *Nat. Rev. Mater.* **2017**, *2*, 17031.
[2] X. Z. Yu, Y. Onose, N. Kanazawa, J. H. Park, J. H. Han, Y. Matsui, N. Nagaosa, Y. Tokura, *Nature* **2010**, *465*, 901.
[3] S. Heinze, K. Von Bergmann, M. Menzel, J. Brede, A. Kubetzka, R. Wiesendanger, G. Bihlmayer, S. Blügel, *Nat. Phys.* **2011**, *7*, 713.
[4] S. Seki, X. Z. Yu, S. Ishiwata, Y. Tokura, *Science* **2012**, *336*, 198.
[5] W. Jiang, P. Upadhyaya, W. Zhang, G. Yu, M. B. Jungfleisch, F. Y. Fradin, J. E. Pearson, Y. Tserkovnyak, K. L. Wang, O. Heinonen, S. G. E. Te Velthuis, A. Hoffmann, *Science* **2015**, *349*, 283.
[6] L. Wang, Q. Feng, Y. Kim, R. Kim, K. H. Lee, S. D. Pollard, Y. J. Shin, H. Zhou, W. Peng, D. Lee, W. Meng, H. Yang, J. H. Han, M. Kim, Q. Lu, T. W. Noh, *Nat. Mater.* **2018**, *17*, 1087.
[7] I. Dzyaloshinsky, *J. Phys. Chem. Solids* **1958**, *4*, 241.
[8] T. Moriya, *Phys. Rev.* **1960**, *120*, 91.
[9] C. Back, V. Cros, H. Ebert, K. Everschor-Sitte, A. Fert, M. Garst, T. Ma, S. Mankovsky, T. L. Monchesky, M. Mostovoy, N. Nagaosa, S. S. P. Parkin, C. Pfleiderer, N. Reyren, A. Rosch, Y. Taguchi, Y. Tokura, K. Von Bergmann, J. Zang, *J. Phys. D: Appl. Phys.* **2020**, *53*, 363001.
[10] J. Grollier, D. Querlioz, K. Y. Camsari, K. Everschor-Sitte, S. Fukami, M. D. Stiles, *Nat. Electron.* **2020**, *3*, 360.
[11] S. Woo, K. Litzius, B. Krüger, M.-Y. Im, L. Caretta, K. Richter, M. Mann, A. Krone, R. M. Reeve, M. Weigand, P. Agrawal, I. Lemesh, M.-A. Mawass, P. Fischer, M. Kläui, G. S. D. Beach, *Nat. Mater.* **2016**, *15*, 501.
[12] W. Jiang, X. Zhang, G. Yu, W. Zhang, X. Wang, M. Benjamin Jungfleisch, J. E. Pearson, X. Cheng, O. Heinonen, K. L. Wang, Y. Zhou, A. Hoffmann, S. G. E. Te Velthuis, *Nat. Phys.* **2017**, *13*, 162.
[13] L. Šmejkal, Y. Mokrousov, B. Yan, A. H. Macdonald, *Nat. Phys.* **2018**, *14*, 242.
[14] J. Barker, O. A. Tretiakov, *Phys. Rev. Lett.* **2016**, *116*, 147203.
[15] W. Legrand, D. Maccariello, F. Ajejas, S. Collin, A. Vecchiola, K. Bouzehouane, N. Reyren, V. Cros, A. Fert, *Nat. Mater.* **2020**, *19*, 34.
[16] H. Jani, J.-C. Lin, J. Chen, J. Harrison, F. Maccherozzi, J. Schad, S. Prakash, C.-B. Eom, A. Ariando, T. Venkatesan, P. G. Radaelli, *Nature* **2021**, *590*, 74.
[17] H. Yang, Y. Sun, Y. Zhang, W.-J. Shi, S. S. P. Parkin, B. Yan, *New J. Phys.* **2017**, *19*, 015008.
[18] K. Kuroda, T. Tomita, M. - T. Suzuki, C. Bareille, A. A. Nugroho, P. Goswami, M. Ochi, M. Ikhlas, M. Nakayama, S. Akebi, R. Noguchi, R. Ishii, N. Inami, K. Ono, H. Kumigashira, A. Varykhalov, T. Muro, T. Koretsune, R. Arita, S. Shin, T. Kondo, S. Nakatsuji, *Nat. Mater.* **2017**, *16*, 1090.
[19] S. Nakatsuji, N. Kiyohara, T. Higo, *Nature* **2015**, *527*, 212.
[20] P. K. Rout, P. V. P. Madduri, S. K. Manna, A. K. Nayak, *Phys. Rev. B* **2019**, *99*, 094430.
[21] J. M. Taylor, A. Markou, E. Lesne, P. K. Sivakumar, C. Luo, F. Radu, P. Werner, C. Felser, S. S. P. Parkin, *Phys. Rev. B* **2020**, *101*, 094404.
[22] Y. Cheng, S. Yu, M. Zhu, J. Hwang, F. Yang, *APL Mater.* **2021**, *9*, 051121.
[23] G. Q. Yan, S. Li, H. Lu, M. Huang, Y. Xiao, L. Wernert, J. A. Brock, E. E. Fullerton, H. Chen, H. Wang, C. R. Du, *Adv. Mater.* **2022**, *34*, 2200327.
[24] H. Yang, A. Thiaville, S. Rohart, A. Fert, M. Chshiev, *Phys. Rev. Lett.* **2015**, *115*, 267210.
[25] A. Belabbes, G. Bihlmayer, F. Bechstedt, S. Blügel, A. Manchon, *Phys. Rev. Lett.* **2016**, *117*, 247202.
[26] Y. Deng, X. Liu, Y. Chen, Z. Du, N. Jiang, C. Shen, E. Zhang, H. Zheng, H.-Z. Lu, K. Wang, *Natl. Sci. Rev.* **2023**, *10*, nwac154.
[27] J. Matsuno, N. Ogawa, K. Yasuda, F. Kagawa, W. Koshibae, N. Nagaosa, Y. Tokura, M. Kawasaki, *Sci. Adv.* **2016**, *2*, 1600304.
[28] C. Sürgers, G. Fischer, P. Winkel, H. V. Löhneysen, *Nat. Commun.* **2014**, *5*, 3400.
[29] A. Gerber, *Phys. Rev. B* **2018**, *98*, 214440.
[30] D. Kan, T. Moriyama, K. Kobayashi, Y. Shimakawa, *Phys. Rev. B* **2018**, *98*, 180408(R).
[31] K. M. Fijalkowski, M. Hartl, M. Winnerlein, P. Mandal, S. Schreyeck, K. Brunner, C. Gould, L. W. Molenkamp, *Phys. Rev. X* **2020**, *10*, 011012.
[32] T. Higo, H. Man, D. B. Gopman, L. Wu, T. Koretsune, O. M. J. van 't Erve, Y. P. Kabanov, D. Rees, Y. Li, M.-T. Suzuki, S. Patankar, M. Ikhlas, C. L. Chien, R. Arita, R. D. Shull, J. Orenstein, S. Nakatsuji, *Nat. Photonics* **2018**, *12*, 73.
[33] W. Wang, Y. Ou, C. Liu, Y. Wang, K. He, Q.-K. Xue, W. Wu, *Nat. Phys.* **2018**, *14*, 791.
[34] X. Li, C. Collignon, L. Xu, H. Zuo, A. Cavanna, U. Gennser, D. Mailly, B. Fauqué, L. Balents, Z. Zhu, K. Behnia, *Nat. Commun.* **2019**, *10*, 3021.
[35] J. Lu, L. Si, Q. Zhang, C. Tian, X. Liu, C. Song, S. Dong, J. Wang, S. Cheng, L. Qu, K. Zhang, Y. Shi, H. Huang, T. Zhu, W. Mi, Z. Zhong, L. Gu, K. Held, L. Wang, J. Zhang, *Adv. Mater.* **2021**, *33*, 2102525.
[36] X. He, N. Helbig, M. J. Verstraete, E. Bousquet, *Comput. Phys. Commun.* **2021**, *264*, 107938.
[37] S. Shimizu, K. S. Takahashi, T. Hatano, M. Kawasaki, Y. Tokura, Y. Iwasa, *Phys. Rev. Lett.* **2013**, *111*, 216803.
[38] S. Rohart, A. Thiaville, *Phys. Rev. B* **2013**, *88*, 184422.
[39] X. S. Wang, H. Y. Yuan, X. R. Wang, *Commun. Phys.* **2018**, *1*, 31.
[40] X. Z. Yu, W. Koshibae, Y. Tokunaga, K. Shibata, Y. Taguchi, N. Nagaosa, Y. Tokura, *Nature* **2018**, *564*, 95.
[41] B. Göbel, I. Mertig, O. A. Tretiakov, *Phys. Rep.* **2021**, *895*, 1.
[42] B. Göbel, A. Mook, J. Henk, I. Mertig, *Phys. Rev. B* **2017**, *96*, 060406(R).
[43] H. Zhou, Z. Wang, Y. Hou, Q. Lu, *Ultramicroscopy* **2014**, *147*, 133.
[44] G. Kresse, J. Furthmüller, *Phys. Rev. B* **1996**, *54*, 11169.
[45] G. Kresse, D. Joubert, *Phys. Rev. B* **1999**, *59*, 1758.
[46] P. E. Blöchl, *Phys. Rev. B* **1994**, *50*, 17953.
[47] J. P. Perdew, K. Burke, M. Ernzerhof, *Phys. Rev. Lett.* **1996**, *77*, 3865.
[48] R. F. L. Evans, W. J. Fan, P. Chureemart, T. A. Ostler, M. O. A. Ellis, R. W. Chantrell, *J. Phys.: Condens. Matter* **2014**, *26*, 103202.
[49] R. F. L. Evans, U. Atxitia, R. W. Chantrell, *Phys. Rev. B* **2015**, *91*, 144425.